256-Channel Magnetic Imaging System[†]

F.C.S. da Silva[a)], S.T. Halloran[b)], A.B. Kos[b)], and D.P. Pappas[b)]

a)*University of Colorado at Denver and Health Sciences Center*

b)*National Institute of Standards and Technology.*

Abstract

We present the design and fabrication of a magnetoresistive imaging system capable of scanning 256 channels simultaneously along linear ranges of either 4 mm or 13 mm. High speed electronics read the channel scans and transfer the data to a computer that builds and displays the images. The system was successfully used to image magnetic tapes for real-time forensic validation purposes and can also be applied in other non-invasive imaging applications.

I.   INTRODUCTION

Imaging the fields generated by magnetic media, e.g., magnetic audio or video tapes, is critical to validating evidence in criminal investigation analysis [1]. The Bitter technique is the conventional way to conduct this analysis [2]. In this method the examiner uses a solution containing solvent and magnetic particles to coat the evidence tape. After the solvent is evaporated, the particles accumulate in areas where the magnetization of the tape changes direction. These areas produce strong field gradients in the direction perpendicular to the tape surface (Fig. 1(a)) and therefore attract the magnetic particles. The examiner observes the particle distribution at the tape surface with an optical microscope.

When implementing the Bitter technique as a forensics tool, it is important to use solutions that can be completely cleaned from the evidence. This limits examiners to the use of relatively large magnetic particles, thereby reducing the spatial resolution. In addition, because the Bitter technique is not sensitive to the polarity of the transition, it is impossible to decode the information. Finally, this technique has a small field of view and is extremely time consuming. It requires examiners to extract the tape, develop the fluid, find the specific event of interest, image it, and clean the evidence. Figure 1(b) shows an image obtained using the Bitter technique. The image is of a 400 Hz stereo sine wave recorded on the top half of a cassette tape and a mono-recording of a stop-head event on the bottom half of the tape.

In a recent publication, Pappas, et al. [3] proposed a novel alternative to the Bitter technique that is non-invasive, sensitive to field polarity, has high spatial resolution, and has the potential to make images as the tape is played. The technique uses a magnetoresistive (MR) scanning head commonly employed in magnetic hard drives (Fig. 1(c).) The head scans across the surface of the magnetic tape to produce high-resolution images. Figure 1(d) shows a MR-head image scan of the same tape used in Fig. 1(b). In this image, we see an improved contrast, spatial resolution, and the polarity of the sine-wave signal.

Despite the improvements, the scanning head technique has many of the same limitations as the Bitter technique, e.g., manual extraction of the tape, small field of view, and long acquisition time. However, the potential for scalability and integration of the scanning head technique associated with fast multi-channel data acquisition systems facilitated the development of a real-time magnetic scanner.

II. DESCRIPTION

In this paper we present the design and fabrication of a high-speed, real-time magnetoresistive imaging system capable of measuring 256 channels per scan with either a 4 mm or 13 mm wide device at an acquisition rate of 8 kscans/s. The host computer controls the acquisition and display of the images and tracks the corresponding audio signature of any channel in real time. It can image magnetic tapes for forensic validation purposes and can furthermore be applied in other non-invasive imaging applications such as imaging current paths in printed circuit boards and integrated circuits.

A photograph of the tape scanning apparatus is shown in Fig. 2. The system uses a modified tape transport from a commercial player. The tape is extracted and passes over both the player head as well as the 256-channel magneto-resistive head. We have developed scanning systems that can image either audio (4 mm wide) or video cassette (13 mm wide) tapes. The heads are interfaced to the preamplifier board via a grid-array of spring-loaded pins housed in a socket that provides mechanical pressure for electrical contacts and head alignment. The system is automated by a computer that controls the audio tape player and the multi-channel head transport into the tape path while it is playing. Calibration of the head is also automated using linear servo motors to move the head over a calibration coil.

A schematic diagram of the system is shown in Fig. 3. Here, the audio tape player or the video tape player interfaces directly with the 256 sensors in the array. The sensor signals are channeled in 16 groups of 16 channels by a multiplexer (mux.) Each group of 16 channels are transferred to an amplifier box and digitized by two 8-channel analog-to-digital converters (ADCs) placed inside the host computer. The ADCs digitize 16 channels in 5 μs or all 256 channels in 80 μs. By defining one scan as 256 channels, the maximum update rate is therefore 12.5 kscans per second. Power for the sensor array is provided by the amplifier box.

III. SENSOR ARRAY

The core of the magnetic imaging system is the sensing element. The MR element maps the amplitude of the magnetic field into a resistance value. The proper operation of an MR sensor depends on several factors. In general, within the range of operation, the

3

MR element should have a linear magnetic response, be hysteresis free, have a dynamic range that is compatible with the measurement requirements, and be able to recover from spikes in temperature and magnetic field. For arrays of MR sensors, additional problems such as cross talk noise (electric and magnetic,) repeatability tolerances, and common-mode rejection (thermal, electric, and magnetic) need to be optimized to ensure proper operation. Below is an itemized description of the sensing element design and how each item addresses the above design rules.

A.   Sensing Element Structure

The magnetic sensing element is composed of an anisotropic magnetoresistive (AMR) layer biased along the easy axis by a tunable exchange-bias multilayer structure [4, 5]. The exchange-bias effect, normally attributed to a ferromagnet-antiferromagnet (FM-AFM) interface [6], is tuned by placing a non-magnetic spacer with adjustable thickness between the FM and the AFM layers.

The optimum bias should maximize the easy-axis hysteresis loop shift and the slope of the hard-axis loop (Fig. 4.) However, the hysteresis loop shift and the hard-axis loop slope have a reciprocal correspondence because a reduction in sensitivity will always occur for higher exchange-bias shifts in the hysteresis curve. As a general design rule, we try to find the minimum exchange-bias shift that removes the hysteresis in the remanent state.

Figure 4 shows the behavior of the exchange-bias shift and the slope of the hard-axis loop for different values of the Ru spacer thickness t in comparison to a sample with no exchange bias. The easy-axis loops in Fig. 4(a-c) show that for increasing values of t, the exchange bias-shift is reduced and that the hysteresis curve approaches the no-bias curve for $t > 1$ nm. Similarly, the slope of the hard-axis loop increases for increasing values of t. A good compromise between these two parameters is $t = 0.5$ nm where the remanent state is non-hysteretic and the slope of the hard-axis loop is not significantly smaller than that of the no-bias sample. Here, the measured shift in the hysteresis curve is 850 A·m^{-1}.

The detailed structure of the sensing element (Fig. 5) starting from the bottom, is Ta (3 nm)/IrMn (8 nm)/Ru (0.5 nm)/Ni$_{81}$Fe$_{19}$ (22 nm)/Ta (3 nm). The bottom Ta layer enhances the adhesion to the substrate. The IrMn layer provides a stable exchange bias and the Ru layer reduces the bias to its optimal value. The AMR layer is composed of a Ni$_{81}$Fe$_{19}$

film deposited in a 16 kA·m^{-1} field along the easy-axis direction. Finally, the top Ta layer protects the AMR layer against oxidation. The substrate is a thermally oxidized (100) Si wafer with a 150 nm oxide layer. The structure is deposited on a lift-off resist patterned wafer and hysteresis curves for the easy and hard axes are measured prior to the lift-off step.

The sensing element geometry is also shown in Fig. 5. Here we chose a needle-shaped element 12.5 μm in length and 2 μm wide for the audio tape head and 43 μm in length and 2 μm wide for the video tape head. These dimensions help the formation of an easy axis in the length direction. In this configuration, the effective lateral or cross-track spatial resolution of the array is 16 μm for the audio tape head and 48 μm for the video tape head.

B. Magnetotransport Properties

Because the fabrication involves many steps and a comprehensive system check can only be performed after the last stage of the process, test devices were designed in unused areas of the sensor chip. These devices, measured after the third metalization layer step, provided the magnetoresistive response of the sensing element in three configurations as shown in Fig. 6. The first configuration is the bare sensing element as defined in Fig. 5. In this configuration, we can measure the effect of the exchange bias effect on the sensitivity of the element and the amplitude of the AMR effect. Figure 7(a) shows the hard-axis AMR response with the resistance tracing a bell-shaped curve versus the external applied field. The exchange bias field H_b can be estimated by considering the sensing element as a single-domain particle. For the curve shown in Fig. 7(a) $H_b = 12.5$ kA·m^{-1} which is more than one order of magnitude higher that the reported value on the wafer level. This discrepancy could be attributed to a series of factors involving magnetostatic interactions and differences in shape, size, and roughness between the film deposited on the photoresist (wafer level) and on the substrate (device level.)

Figure 6(b) shows the second test device configuration which is the building block of the actual sensing cell in the sensor array. In this configuration, barber-pole lines were placed on the sensing element to linearize the magnetic field response of the resistance around zero field. The barber-pole lines are positioned at a 45° angle with respect to the long axis of the sensing element. By selecting a material much more conductive than Ni$_{81}$Fe$_{19}$ such as Al, the barber-pole lines can bias the direction of the current inside the AMR layer at 45°. The

corresponding response is shown in Fig. 7(b) where a linear range in the MR curve between -5 kA·m^{-1} and $+5$ kA·m^{-1} is observed. Outside this range, the asymmetry in the curve can be attributed to the fact that the current is not symmetrically distributed around 45°. Therefore, lines placed at a -45° angle would generate a response equivalent to a change in the sign of the applied field of Fig. 7(b).

By combining four barber-pole AMR elements in a bridge configuration as shown in Fig. 6(c), the sensing cell produces a symmetric response to the magnetic field (Fig. 7(c)). On each leg of the bridge, two barber-pole sensing elements with current bias angles of $+45$° and -45° ($+-$ for simplicity) produce twice the resistance change of a single element. The bias sequence on each leg alternates ($+-$ and $-+$) in order to provide a differential signal that is proportional to the applied field. The bridge is designed to reject first-order thermal, electrical, and magnetic common modes provided that the resistance of the elements are matched to within ± 5 %. The thermal common mode rejection comes from the proximity of the sensors and how fast heat propagates in the system. Finite element analysis simulations show that 100 K temperature spikes above the background occurring 4 μm from the edge of the sensors are sensed by the two elements (5.5 μm apart) in less than 10 μs. This time window limits the maximum acquisition rate to 50 kHz according to Nyquist's theorem. Finally, the magnetic noise rejection is effective provided that magnetic field gradients are smaller than 180 kA·m^{-1}/m. This figure is obtained by dividing the sensing element noise floor at 10 kHz (≈ 1 A·m^{-1}) by the distance between elements (5.5 μm.) This limit is much higher than 10 A·m^{-1}/m, which is the gradient of a 100 nm film with a saturation magnetization of 8×10^5 A·m^{-1} measured at a height of 4 μm.

C. Fabrication

The fabrication of the sensor array uses standard patterning, deposition and etching processes. The specific choice of process and layout rules used here depended on the level of component integration, critical feature size, and repeatability of the pattern that ultimately affects the yield of each channel of the array. We designed and fabricated fourteen masks using a 1 μm-resolution pattern generator and chrome-coated soda-lime plates. Table I describes the process steps using each mask.

The metallic layers were deposited using sputtering and electron-beam evaporation. The

SiO$_2$ insulating layers, deposited by plasma enhanced chemical vapor deposition (PE-CVD,) provided a conformal coating of the metallic layers and low density of pinholes in the oxide.

Two dry-etch methods were used in the fabrication: a regular reactive ion etch (RIE) for the insulator layer and a deep reactive ion etch (DRIE) for cutting an edge line on the Si wafer 4 μm from the linear sensor array. The sputter-deposited Al layers were etched using an alkaline etching solution. Ar plasma or ion-mill cleaning steps were performed before each deposition.

The patterning exposure used an I-line stepper in two types of positive resist and a double-layer combination of positive and lift-off resist. The smallest feature (barber-pole line) was 0.7 μm in size and the positioning was better than 50 nm (nominal).

The fabrication tolerances and design rules described above accounted for arrays with less than 5 % of variation in the element resistance and 16-bit dynamic range at 8 kscans/s. These results were obtained by measuring bridge offset from the transfer curves of all elements in the array.

IV.   ELECTRONICS MODULE

The sensing cell described in Fig. 6(c) has a 32 μm long footprint (96 μm for the video tape head) and individually represents one channel. The schematic diagram of this full-step bridge is shown in Fig. 8(a) and the voltage of each channel i, $V_{\mathrm{ch}\,i}$ is given by:

$$V_{\mathrm{ch}\,i} = V_{2i} - V_{2i-1}, \tag{1}$$

where $1 \leq i \leq N$, and N is the total number of bridges.

With the same number of bridges, we can measure twice as many channels by using an interleaved or half-step bridge configuration shown in Fig. 8(b). The voltage of each channel is now given by:

$$V_{\mathrm{ch}\,i} = (-1)^i (V_i - V_{i-1}) \tag{2}$$

Here, $V_{\mathrm{ch}\,0} \equiv 0$ and therefore $V_{\mathrm{ch}\,1} = V_1$. Equation 2 describes a system of $2N$ linear equations and $2N$ unknowns. The system is computationally fast to solve because it involves only additive operations provided that there is no crosstalk between the channels. One source of electrical crosstalk is the resistance between the power planes and the bridge sensing elements. However, resistance network simulations showed that if the power plane resistance

is less than 0.1 Ω the crosstalk decreases to the same levels of the sensing element noise floor. All barber-pole lines, power planes, and voltage connections were therefore fabricated using Al as a connecting metal.

Figure 9 shows the sensitivity of each element in the array with respect to the sensor index. The sensitivity is defined as the slope of the straight line that interpolates the sensor response to the magnetic field in the linear regime and is reported here in mV/T units. A histogram (Fig. 9 inset) shows that 80 % of the sensitivities are within one standard deviation from the average 25.5 mV/T with the exception of a few channels that were saturated. These affected channels were 2 % to 3 % of the total number of channels. An estimate of the magnetic field for these channels is approximated by the averaging of the adjacent channels. Figure 9 also shows that the non-uniformities in the sensitivities are systematic and symmetric. This systematic symmetry is a consequence of inhomogeneities in the calibration field or in the current distribution across the bridges which changes the current-induced bias in the barber-poles [7]. The sensitivity data are used to calibrate the magnetic field measurements of each sensor and therefore provide a uniform linear response of the array.

The interface between the sensor array channels and the electronics module shown in Fig. 10 describes the signal path from bridges in the sensor array to the acquisition cards placed in the host computer. The electronics consists of a socket board to isolate the different channels, a multiplexer board that serves to preamplify the signals and multiplex them onto 32 (16 differential pairs) channels, and a filter board where they are further amplified and the high frequency components are removed. The filter board outputs the 32 channels of signal to the two analog-input data acquisition boards. The filter board also provides power to the sensor array and the connections to the host computer are made using standard 68-pin SCSI connectors.

The socket board is an eight-layer board with a custom socket designed to hold a single 13 mm × 13 mm die containing the 256 element magnetoresistive array and the test structures. The output pads for the 256 differential signals are in an 18×18 pad matrix with 600 μm by 700 μm spacing. The extra pads are used for bias current. The die is loaded into the socket with the pads facing down so that they will make contact with the spring-loaded (pogo) pins and the array stripe aligned with the opening in the socket. These pins interface with pads on the board where the 256 differential channels are broken out. Connection to the

multiplexer board is through two 4×21 connectors with 2 mm spacing.

The multiplexer board is the first stage of signal processing. The 256 differential channels are fed into sixteen differential multiplexers. The multiplexed differential voltages, which follow Eq. 2, provide the input of the preamplifier stage. Four lines of digital input from a high speed digital input/output card are programmed to step through the multiplexers in the correct order. High precision, low noise operational amplifiers, used in a differential configuration, move the signal level away from the noise floor. The multiplexer board sends the differential channels to the filter board that is inside the electronics enclosure through a 68 conductor ribbon cable. We found that the time to settle at the preamp stage is close to 2 μs for a voltage swing of 50 mV.

The filter board takes in the differential voltages, amplifies the signal with a high speed, programmable gain instrumentation amplifier (PGA) where the gain is programmed with two channels of the high speed digital input/output card. This feature maintains the maximum dynamic range into the analog-to-digital converters on the input cards. The final signal processing stage is a differential Sallen-Key filter [8] with a roll-off near 300 kHz.

The differential output of the Sallen-Key filter is then sent to a data acquisition card where the signals are digitized and processed further in software. The acquisition cards read eight channels of differential analog signals at a sampling rate of 25 ksamples per second which represents an aggregate sampling bandwidth of 200 kHz. The average cassette tape speed is approximately 5 cm/s. At 25 ksamples per second, each scan is spatially separated by 2 μm. This is the real-time spatial resolution of the magnetic imaging system. Finally for a voltage swing of 2 V a settling time of less than 4 μs can be achieved which is equivalent to a 250 kHz maximum sampling bandwidth.

The filter board also contains the current source for the bridges and the power regulating electronics. Further conditioning is provided at the point-of-load regulators on the multiplexer board. All differential signal traces on the three boards have minimum pickup loops to reduce external noise. Analog and digital ground planes are kept separate and all connecting cables are arranged to isolate digital lines from analog lines. The potentiometer on the front of the electronics enclosure regulates the current driving the sensing bridges.

After the signal from the bridges is converted into a 16-bit digital format, the host computer organizes the information and displays each channel as a horizontal trace where the shade of gray defines the amplitude of the signal (black and white for a saturated negative

9

and positive signal) in the time domain (horizontal axis.)

V. SOFTWARE

The software interface combines four main modules that helps the operator configure and calibrate the hardware, acquire and analyze images. The modules names are: *calibration, player controls, plotting, and important variables.* In the *calibration* module, setpoints for the bridge voltage and channel amplifier gain are entered. In addition, operating parameters such as sensitivity and bridge offset for each channel are measured and stored.

The *player controls* module helps the operator adjust the home positions of the head for the image scan acquisition. A virtual tape deck with the "play", "stop", "pause", "fast forward", and "rewind" buttons assists the operator in imaging the relevant sections of the tape for the analysis. Here, when the "play" button is pressed, the acquisition window opens to show, in real time, the acquired image scan as the corresponding audio is played. The new window controls the play volume and has basic image manipulation and data extraction functionalities that help the operator isolate and characterize, in situ, the recently acquired image.

A more detailed and comprehensive set of image manipulation and data analysis functions are present in the *plotting* module (Fig. 11) for the analysis of current or previously acquired scans. In this module, the operator can switch to other modules via the module tab bar (Fig. 11(a)) and turn on and off the application window in the main control toolbar (Fig. 11(b)). The image manipulation toolbar (Fig. 11(c)) can read and save previously acquired scans, zoom into a specific area of the image or visualize the entire scan, and change the color palette and contrast of the image. The data manipulation toolbar (Fig. 11(f)) manages four analysis tools. The first, shown in the image window, is a two-dimensional color map of the cross track versus downtrack field amplitude called the image window. In the image window shown in Fig. 11(d) a gray scale shows negative field values pointing toward black and positive field values pointing toward white. The second is the channel downtrack scan line, a two-dimensional plot (Fig. 11(e)) showing the amplitude of the magnetic field measured by a single channel selected via a horizontal dotted line in the image window. The cross-track scan line (Fig. 11(g)) provides the magnetic field measured as a function of the channel index in the direction perpendicular to the tape movement. A vertical dotted line assists

10

the operator in selecting the position for the cross-track line scan. Finally, the average scan tool performs a spatial average of the cross-track data bound by two horizontal dashed lines in the image window. The average is plotted (Fig. 11(h)) as a function of the position in a range defined by two vertical dashed lines.

VI.   APPLICATIONS

Figure 12 shows the image of an audio tape obtained by the audio tape head. The image focuses on one of the sides where an audio signal was previously recorded. The audio was partially erased by the same recording head and characteristic mark was left when the recording head was removed. In forensic analysis the head stop mark is an indication that the tape was altered and helps determine the validity of the evidence.

The important aspect of this image is that it was taken while the tape was being played. The captured event was triggered by the operator when the discontinuity was heard. In addition, the software allows the operator to play back the signal from any given selection of the tape. This is a powerful new addition to the tape forensics toolbox. Finally, it is possible to digitally image the entire tape. Given a storage requirement of 8 Mbyte of data per second of audio, it would require only 43 Gbytes to store the image of a typical 90-minute tape.

Figure 13(a) shows a one-second scan of a cassette tape imaged with the 256-channel sensor array. At the bottom half of the scan the figure shows three regions. Region I shows the typical image signature of a stereo audio pattern. The audio was erased in region II where a sharp interface marks the start of an erase head event. Region III highlights the erase head stop event. Figure 13(b) show in detail the erase stop event measured with the sensor array in comparison to the same section imaged using the Bitter technique (Fig. 13(c)). The erase stop event has a magnetic pattern that is unique for each type of tape recorder (brand and model) and can be seen in more detail by the 256-sensor array.

Figure 14 shows the image of a video tape where we can see the stereo audio traces at the bottom, the video signal covering most of the image in the middle, and the synchronization marks at the top. The grey scale follows the polarity of the field so that black and white represent the saturation state of the sensor in opposite directions respectively. Both audio channels could be recovered by simply converting the image digital data into an analog

signal output to a speaker. These images are acquired as the examiner views and listens to the tape. Again, the acquisition stops when an event is seen on the scan or heard by the examiner.

VII. SUMMARY

We have demonstrated a system that is capable of imaging magnetic tape recording head events in real time. A thorough description of the system provided in this paper shows how reliable the system can be in imaging magnetic tape for forensic purposes. Other potential applications of the system include current mapping of printed circuit boards and semiconductor chips, stress and fracture analysis, and magnetic bead sensing for biological systems. One audio tape imaging system unit has been delivered to the Federal Bureau of Investigation, and is currently being validated for use in authentication of evidence for forensic investigation purposes.

---

[1] B.E. Koenig, J. Audio Eng. Soc. **38**, 3 (1990).

[2] N.H. Yeh, IEEE Trans. Magn. **16**, 979 (1980).

[3] D.P. Pappas, A.V. Nazrov, D. Stevenson, S. Voran, M.E. Read, E.M. Gormley, J. Cash, K. Marr, and J.J. Ryan, J. Elec. Imag. **14**, 013015 (2005).

[4] D. Wang, J. Daughton, C. Nordman, P. Eames, and J. Fink, J. Appl. Phys. **99**, 08H703-1 (2006).

[5] S.T. Halloran, F.C.S. da Silva, H.Z. Fardi, and D.P. Pappas, J. Appl. Phys. **102**, 033904 (2007).

[6] See, for example, J. Nogues, and I.K. Schuller, J. Magn. Magn. Mat. **192**, 203 (1999).

[7] S. Tumanski in Thin Film Magnetoresistive Sensors p. 22, IOP Publishing Ltd 2001.

[8] see, for example, P. Horowitz and W. Hill, "The Art of Electronics", Cambridge University Press, 267 (1989). ISBN 0 521 37095

Step	Depositions	Etches	Liftoffs
Alignment Marks	none	RIE	none
Power Plane 1	Al (sputtering)	wet	none
AMR Layer	Ta/IrMn/Ru/NiFe/Ta (sputtering)	none	yes
AMR Contacts	Al (e-beam)	none	yes
Via 1	SiO_2 (CVD)	RIE	none
Power Plane 2	Al (sputtering)	wet	none
Via 2	SiO_2 (CVD)	RIE	none
Contact 1	Al (sputtering)	wet	none
Via 3	SiO_2 (CVD)	RIE	none
Contact 2	Al (sputtering)	wet	none
Via 4	SiO_2 (CVD)	RIE	none
Platting	Ti/AuPd (e-beam)	none	yes
Dicing	none	DRIE	none

TABLE I: Processes involved in the fabrication of the sensor array. The first column describes the individual lithographic steps. If the step is a deposition, the second column shows the deposited material and in parenthesis the deposition method. If the step requires an etch, the third column shows the etch method. The fourth column indicates whether the step is a lift-off step or not.
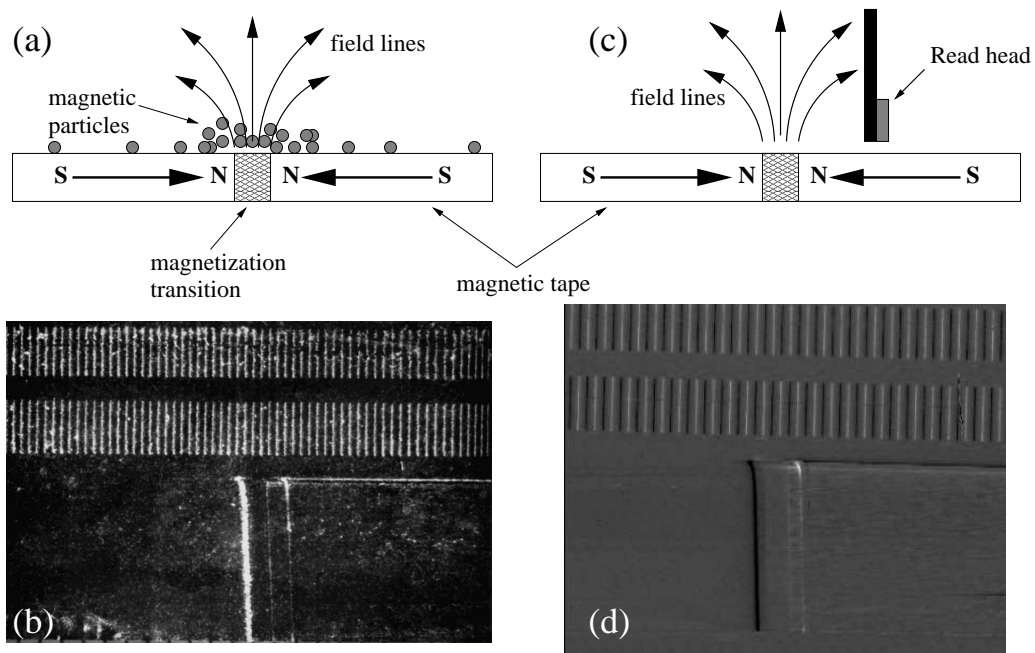
FIG. 1: Comparison between the Bitter technique (a,b) and the scanning read head technique (c,d). The diagrams illustrate the principle of operation for the (a) Bitter and (c) read head techniques. The images show the results obtained by scanning the same tape using the b) Bitter and d) read head techniques.
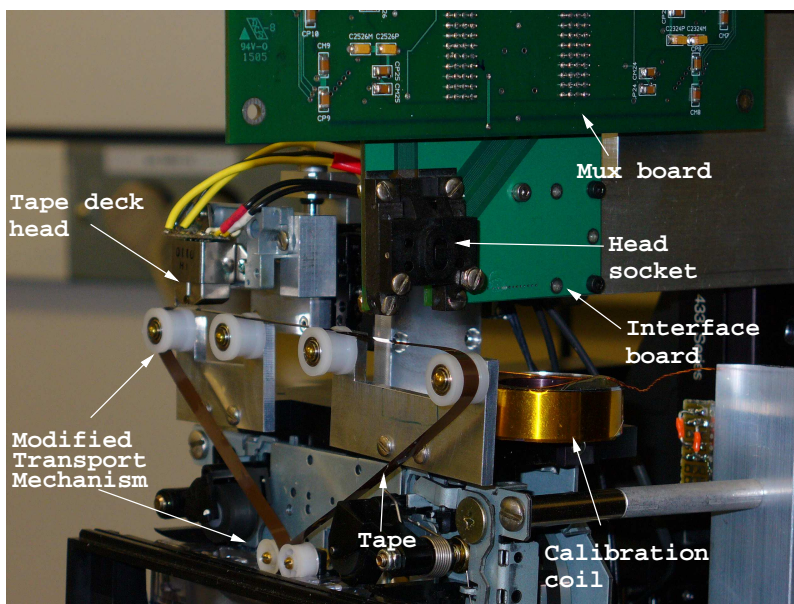
FIG. 2: Photograph of the transport mechanism used in the imaging of audio tapes.

16 x 16 Mux

13 mm head

Video tape player

Power supply
+
Amplifier Box

Computer:
– Labview
– 16 analog input
– Digital output

16 x 16 Mux

conventional
head

4 mm head

Tape transport

Audio tape player
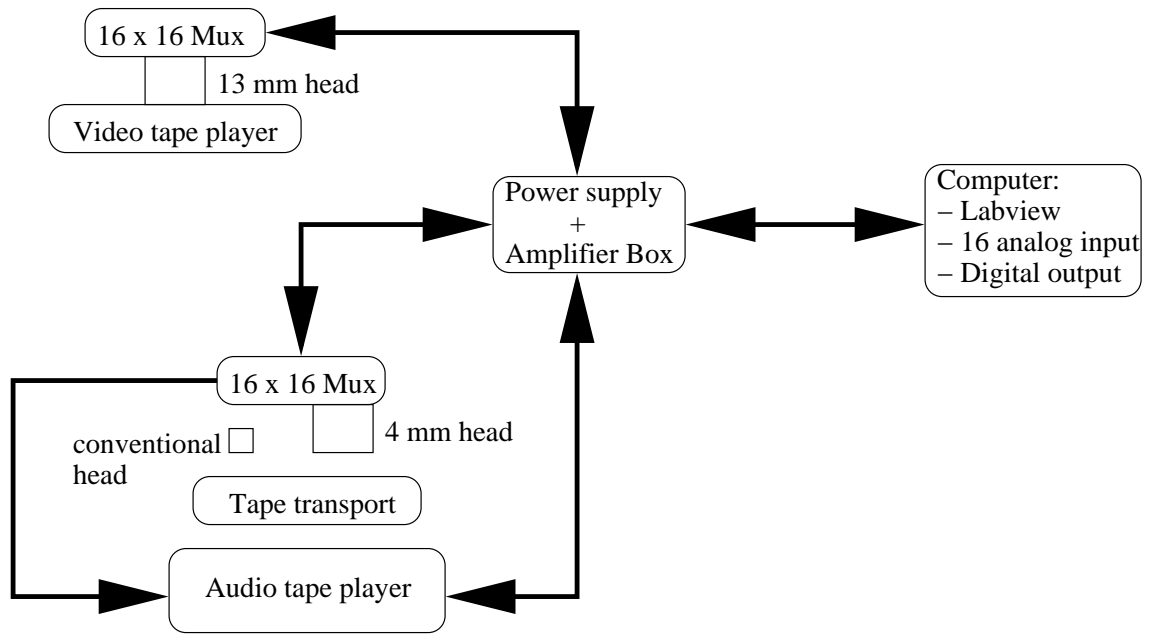
FIG. 3: Schematic diagram of the imaging system.
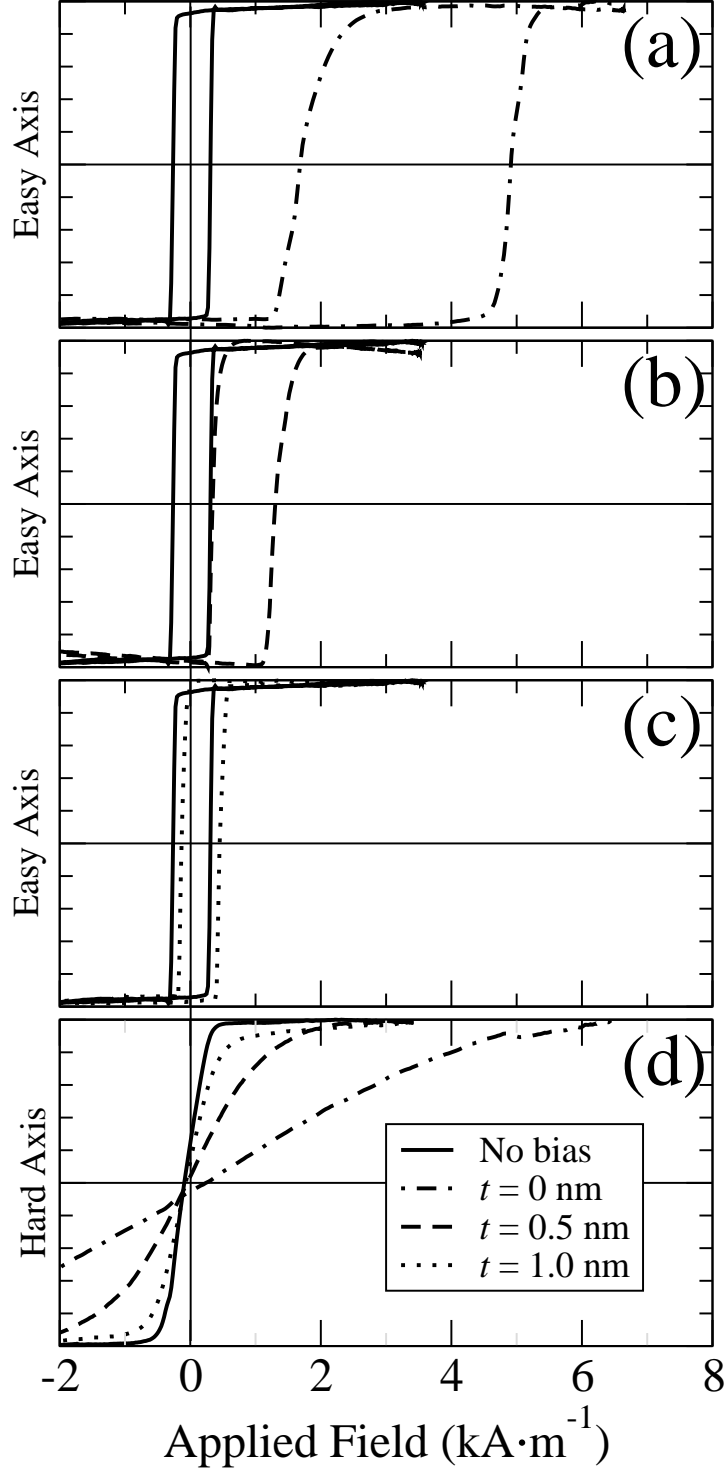
FIG. 4: Normalized hysteresis loops showing a comparison between samples prepared with different thicknesses t of the Ru spacer (dotted lines) and the no exchange bias sample (solid lines.) The dotted lines in the easy-axis loops (a-c) correspond to $t = 0$ nm, 0.5 nm, and 1.0 nm respectively. The hard-axis loops are shown in (d).

Ta (3 nm)		
NiFe (23 nm)	2 μm	
Ru (0.5 nm)		
IrMn (8 nm)		
Ru (8 nm)		
Ta (3 nm)		
SiO$_2$ (150 nm)	2 μm	
Si substrate		

Cassette element

bias

hard axis

easy axis

12.5 μm

VHS element

bias

hard axis

easy axis

43 μm
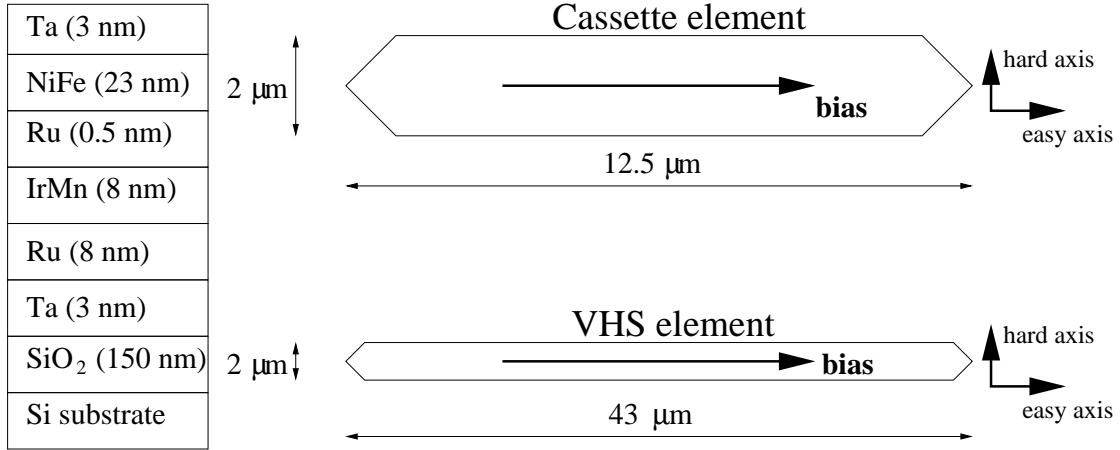
FIG. 5: Schematic side view of the multilayered structure of the sensing element (left) and the geometry of the sensing element for the Cassette (top right) and Video (Bottom right) sensor array.

(a)

I+

I−

(b)

I+

I−

H

(c)

I+
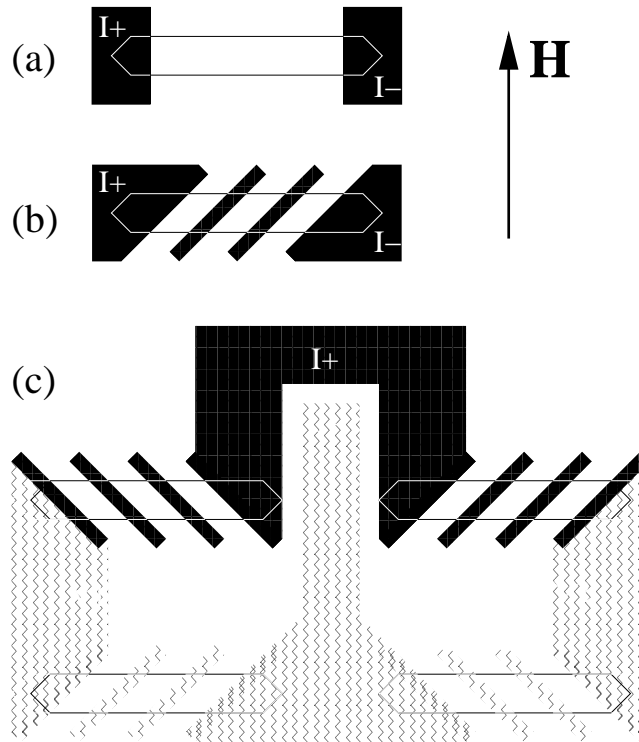
FIG. 6: To-scale physical layout diagram of the test structures fabricated on idle areas of the sensor array: (a) Single element, (b) single barber-pole, and (c) barber-pole bridge. The sensed magnetic field **H** is perpendicular to the long axis of the sensing elements.
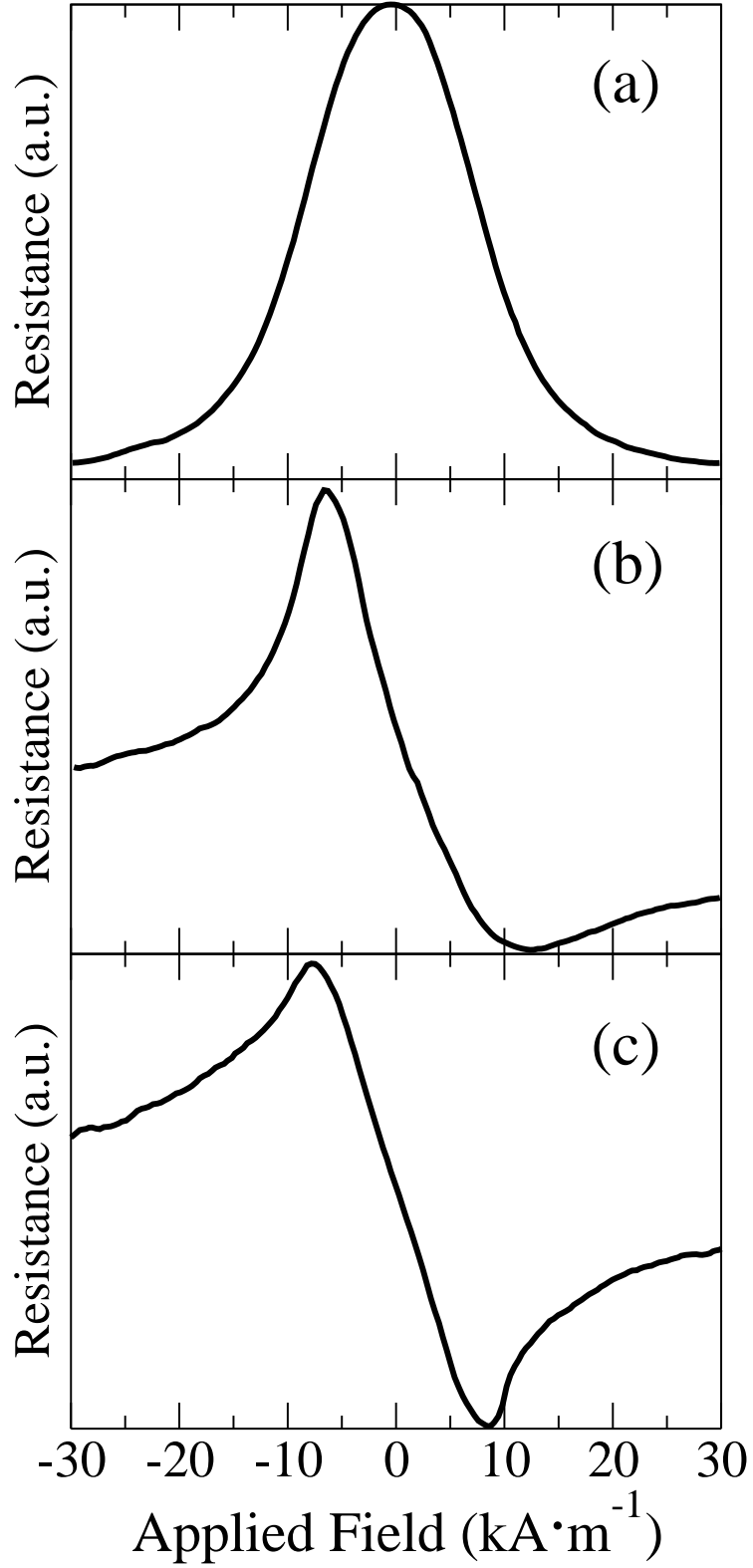
FIG. 7: Experimental magnetoresistance curves measured for the (a) single element, (b) single barber-pole, and (c) barber-pole bridge as a function of the external applied field as described in Fig. 6.
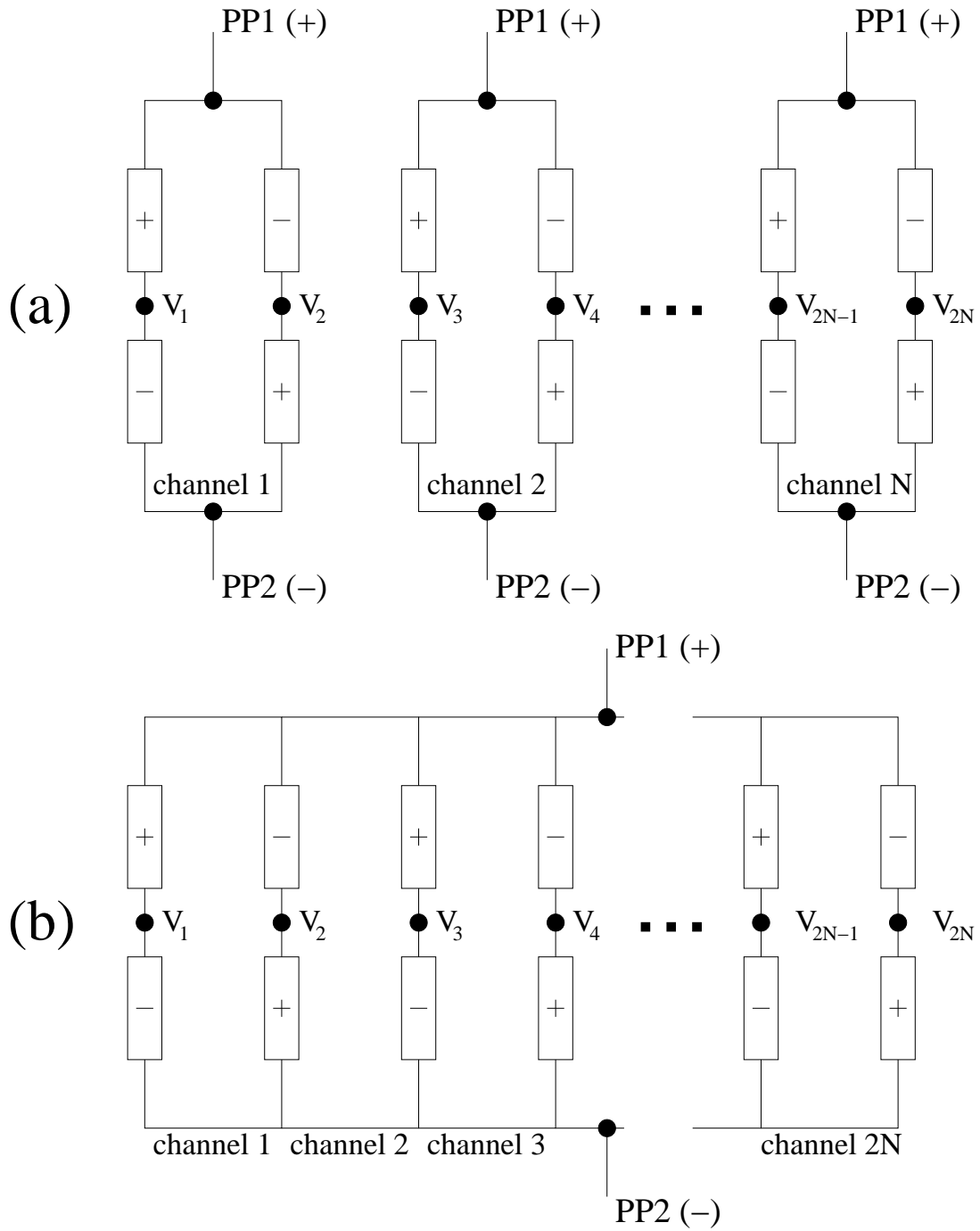
FIG. 8: Schematic diagram of the (a) full-step bridge and b) half-step bridge configurations.
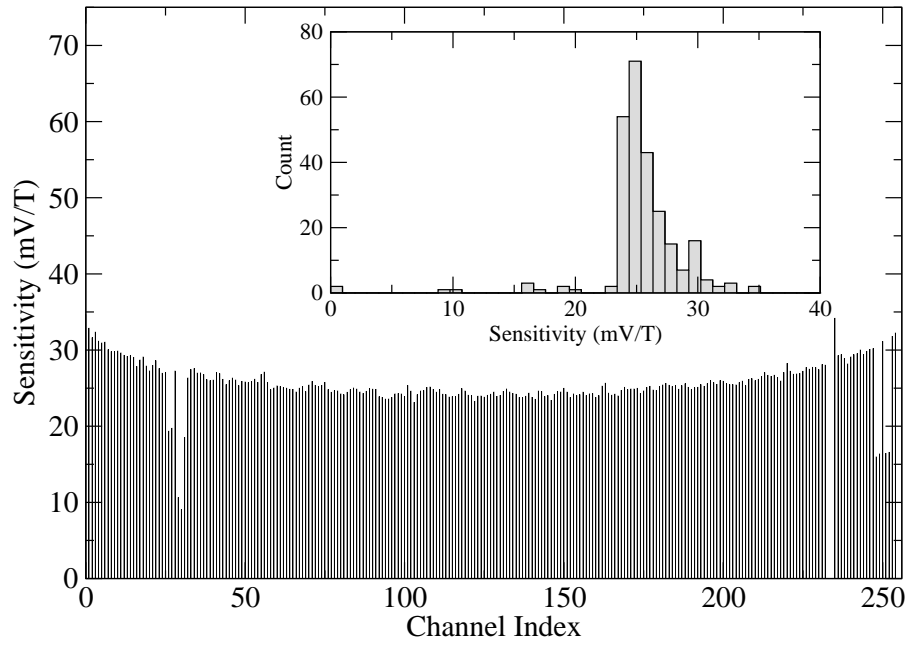
FIG. 9: Magnetic field sensitivity of the elements in the sensor array and the corresponding sensitivity histogram (inset.)
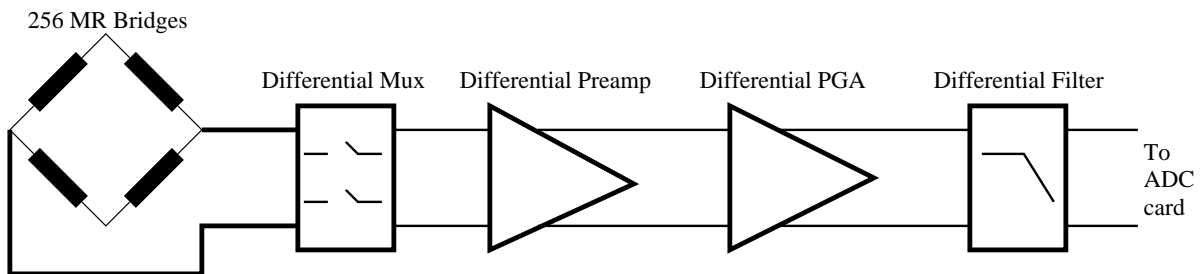
FIG. 10: Diagram showing the flow of the signal through the electronics module.
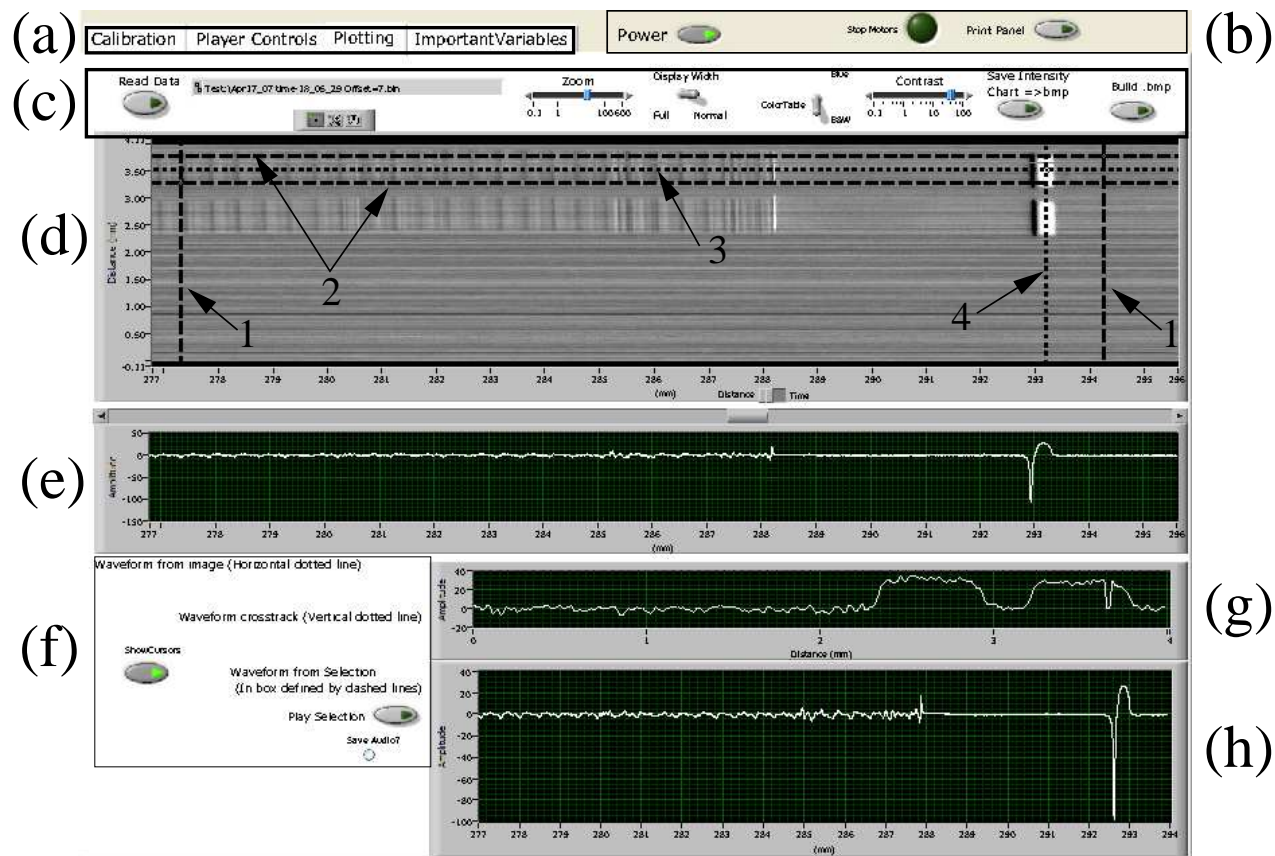
FIG. 11: Screenshot of the software interface in the *plotting* module where we can see: (a) the module tabs; (b) the main control toolbar; (c) the image manipulation toolbar; (d) the image window: (1) the average scan horizontal delimiter lines, (2) the average scan horizontal delimiter lines, (3) the channel downtrack scan line, (4) the cross-track scan line; (e) the individual channel downtrack scan window; (f) the data manipulation toolbar; (g) the cross-track scan window; and (h) the downtrack average scan window.
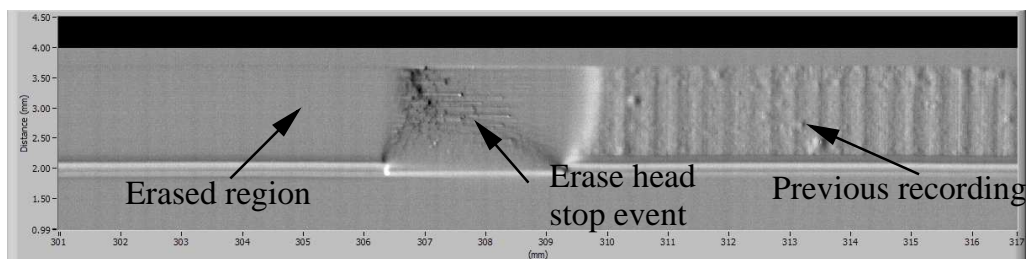
FIG. 12: Image of an audio tape obtained with the audio tape head.
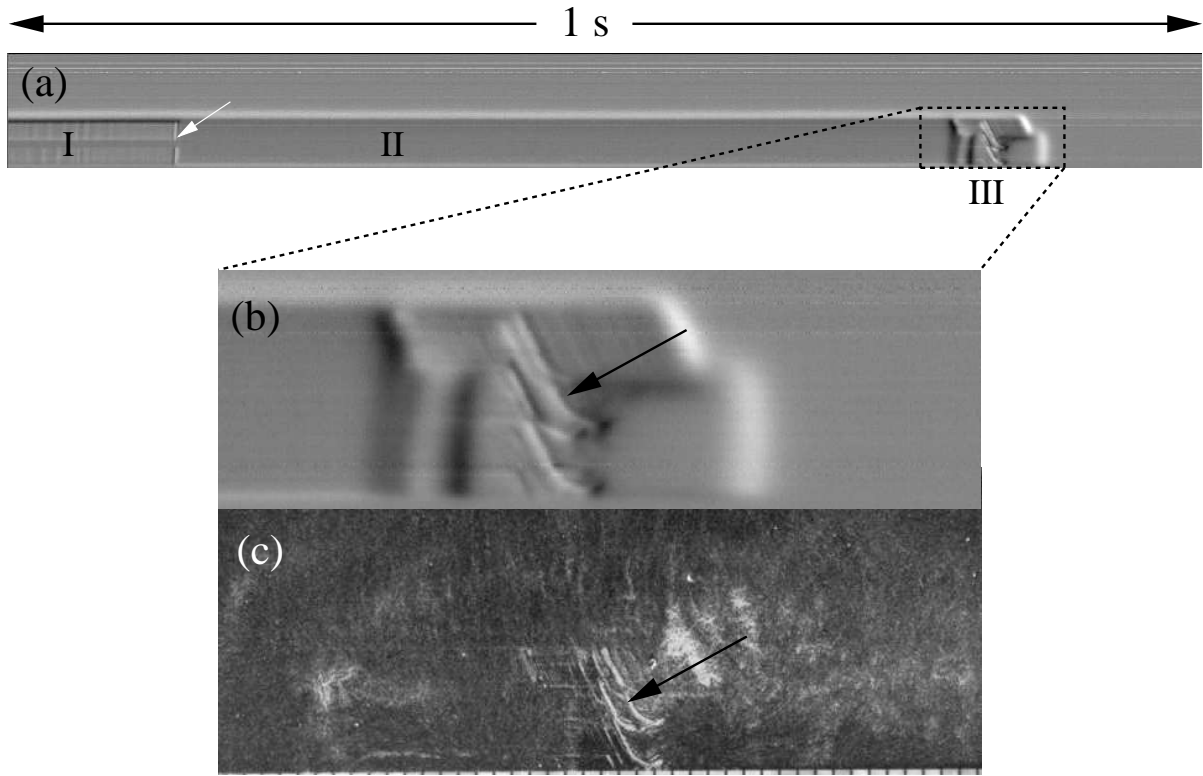
FIG. 13: (a) One second of audio in a cassette tape imaged using the 256-sensor array: (I) regular audio signature, (II) erased region, and (III) erase head stop event. The white arrow indicates the erase mark starting point. The dotted rectangle highlights the erase stop event showed in detail in (b) and compared with the Bitter technique (c). The black arrows indicate the recorder signature marks.
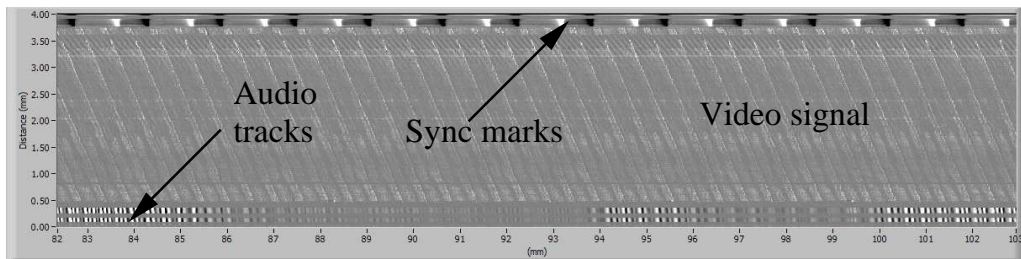
FIG. 14: Image of a video tape obtained with the 256-sensor video tape head.